Earth and Planetary Science Letters 526 (2019) 115784

Contents lists available at ScienceDirect

Earth and Planetary Science Letters

www.elsevier.com/locate/epsl

Influence of ring faulting in localizing surface deformation at subsiding calderas

Yuan-Kai Liu [a,b], Joël Ruch [a,c], Hannes Vasyura-Bathke [a,d], Sigurjón Jónsson [a,*]

[a] Physical Sciences and Engineering Division, King Abdullah University of Science and Technology (KAUST), Thuwal 23955, Saudi Arabia
[b] Now at Seismological Laboratory, California Institute of Technology, Pasadena, CA 91125, USA
[c] Now at Department of Earth Sciences, University of Geneva, 1205 Geneva, Switzerland
[d] Now at Institute of Geosciences, University of Potsdam, 14476 Potsdam, Germany

A R T I C L E I N F O

Article history:
Received 26 March 2019
Received in revised form 16 August 2019
Accepted 18 August 2019
Available online 4 September 2019
Editor: T.A. Mather

Keywords:
volcanic deformation
ring faulting
caldera collapse
analog models
boundary element modeling
InSAR

A B S T R A C T

Caldera unrest can lead to major volcanic eruptions. Analysis of subtle subsidence or inflation at calderas helps understanding of their subsurface volcanic processes and related hazards. Several subsiding calderas have shown similar patterns of ground deformation composed of broad subsidence affecting the entire volcanic edifice and stronger localized subsidence focused inside the caldera. Physical models of internal deformation sources used to explain these observations typically consist of two magma reservoirs at different depths in an elastic half-space. However, such models ignore important subsurface structures, such as ring faults, that may influence the deformation pattern. Here we use both analog subsidence experiments and boundary element modeling to study the three-dimensional geometry and kinematics of caldera subsidence processes, evolving from an initial downsag to a later collapse stage. We propose that broad subsidence is mainly caused by volume decrease within a single magma reservoir, whereas buried ring-fault activity localizes the deformation within the caldera. Omitting ring faulting in physical models of subsiding calderas and using multiple point/sill-like sources instead can result in erroneous estimates of magma reservoir depths and volume changes.

1. Introduction

Volcanic deformation is commonly associated with changes in underlying magma reservoirs and plumbing systems (De Natale et al., 1997; Segall, 2010) and is often observed as inflation or deflation during episodes of eruption or unrest. Geodetic techniques, such as GPS and satellite-based interferometric synthetic-aperture radar (InSAR) imaging are the primary tools to monitor ground deformation on active volcanoes today (Pyle et al., 2013; Biggs et al., 2014). Observed displacements are then typically used to constrain analytical or numerical models of possible deformation sources in an elastic half-space, representing pressurization in magma bodies of some shapes such as spheres, vertical dike intrusions, and horizontal sills. The estimated parameters of the deformation sources are then interpreted as properties (dimensions, geometries, volume changes, etc.) of the crustal magma bodies in nature (Dzurisin, 2003; Poland et al., 2006; Segall, 2010).

Caldera collapse, induced by a major depletion of a magma reservoir, is probably the most notable type of volcanic deformation (Cole et al., 2005; Acocella, 2007). However, caldera collapses are rarely witnessed and calderas typically only experience subtle deformation in response to magma activity at depth. Interestingly, several deforming calderas have shown a similar surface deformation pattern observed by InSAR after changes in subsurface magma reservoirs or following small- to moderate-size eruptions. The pattern manifests overlapping deformation signals, composed of broad deflation affecting the entire volcano edifice and of localized subsidence concentrating within the caldera depression (Peltier et al., 2009; Chadwick et al., 2011; Bagnardi and Amelung, 2012; Xu et al., 2016; Holohan et al., 2017). One intriguing example was related to the 2015 Wolf volcanic eruption, Galápagos, where 60 cm coeruptive intracaldera subsidence was observed, superimposed on a smoother edifice-wide subsidence extending about 12 km from the center of the caldera (Fig. 1). Modeling of the observed deformation showed that two shallow magma reservoirs, located at ∼1 km and ∼5 km below sea level under Wolf, explained the deformation signals (Xu et al., 2016). At another Galápagos caldera, Fernandina, observed ground deformation before and after an eruption in 2005 showed a similar overlapping deformation pattern (Chadwick et al., 2011;

* Corresponding author.
E-mail address: sigurjon.jonsson@kaust.edu.sa (S. Jónsson).

https://doi.org/10.1016/j.epsl.2019.115784

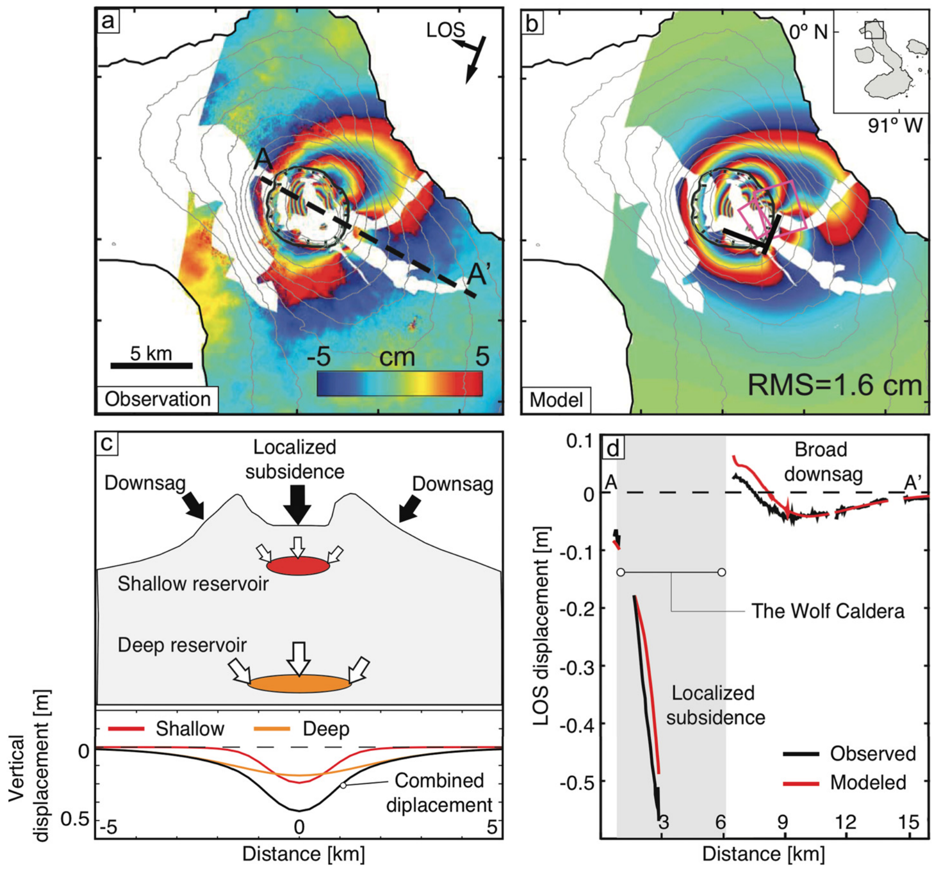

Fig. 1. Overlapping surface deformation patterns observed at Wolf volcano, Galápagos, modified from Xu et al. (2016). (a) Co-eruptive InSAR data (ALOS-2, descending orbit) of the 2015 Wolf eruption spanning 42 days (22 May–3 July), with each fringe corresponding to 10 cm line-of-sight (LOS) displacement. The InSAR data show concentrated subsidence within the caldera superimposed on a broad subsidence signal affecting the entire volcanic edifice. (b) A model that includes two sill-like magma reservoirs (purple rectangles) and two eruptive dikes (thick black lines) can approximately reproduce the deformation pattern. (c) Illustration of the two-reservoir model and the corresponding vertical displacements composed of long- and short-wavelength subsidence. (d) The observed (black) and modeled (red) displacements along profile A-A' shown in (a).

Bagnardi and Amelung, 2012). As in the Wolf case, the concentric superimposed deformation was modeled by using two magma reservoirs at different depths below the caldera: a shallow sill at ∼1 km depth and a deeper point source at ∼5 km depth below sea level.

Although the overlapping deformation signals observed at several subsiding calderas can be explained by models of multiple magma reservoirs at different depths (Table 1), such models usually assume simple point or sill-like sources in an elastic half-space (Chadwick et al., 2011; Bagnardi and Amelung, 2012; Xu et al., 2016). Furthermore, they do not take into account fracture systems in the host-rock under calderas, such as ring faults. Ring faults are subsurface structural boundaries of calderas and their activity has been extensively studied at both active and extinct volcanoes through seismic datasets (Mori and McKee, 1987; Ekström, 1994; Mori et al., 1996), geologic evidence (Geshi et al., 2002; Michon et al., 2007), and laboratory experiments (Roche et al., 2000; Acocella, 2007; Holohan et al., 2008, 2011; Burchardt and Walter, 2010; Howard, 2010; Ruch et al., 2012). The importance of ring faults in influencing ground deformation episodes was explored and modeled in three dimensions in a study of the Campi Flegrei caldera, Italy, showing that mechanically weak ring faults might localize surface deformation within the caldera (Beauducel et al., 2004). In addition, localized and sharply bounded deformation observed within the calderas of Tendürek volcano in Turkey (Bathke et al., 2015) and Bárðarbunga volcano in Iceland (Gudmundsson et al., 2016) was related to buried ring-fault activity. Furthermore, Xu et al. (2016) suggested that the overlapping surface deformation signals observed during the Wolf eruption might potentially be due to depletion of a single magma reservoir combined with the activity of a buried ring fault.

Similar inferences were made for Piton de la Fournaise, La Réunion, where observed volcanic deformation was seemingly caused by pressure changes within several reservoirs (Peltier et al., 2009). The estimated reservoir depth changed from a depth of ∼2 km during uplift before the April 2007 eruption, to ∼1 km following the eruption and then to only ∼0.4 km later during the post-eruption subsidence. As ring faulting was observed (Michon et al., 2007), Peltier et al. (2009) compared pressure source modeling in different media and suggested that deflating sources surrounded by a fractured medium would generate more localized ground deformation than similar sources within a homogeneous medium. This topic was further explored with discontinuum mechanics models by Holohan et al. (2017), who proposed that the inferred changes of shape, orientation, and depth of the magma reservoirs associated with the 2007 eruption were primarily related to inelastic host-rock deformation initiating from a deep magma reservoir and then migrating upward before eventually reaching the surface. Thus, using a homogeneous host-rock assumption may lead to misestimation of the depth of magma reservoirs (Peltier et al., 2009).

Here we study further the localization effect ring-fault activity may have on volcanic deformation and explore whether it can explain the observed overlapping surface deformation patterns seen at several deforming calderas. Our analysis is based on two complementary approaches: analog laboratory experiments and computer-based boundary element modeling. In addition, we dis-

Table 1
Several cases of overlapping deformation patterns at calderas.

Volcano	Data	Interpretation	Reference
Campi Flegrei (Italy)	InSAR, leveling	One spherical source, ring fault	Beauducel et al., 2004
Sierra Negra (Galápagos)	InSAR	Trapdoor faulting	Jónsson et al., 2005
Fernandina (Galápagos)	InSAR, GPS	One sill, one point source, one dike	Chadwick et al., 2011
	InSAR	Two sills	Bagnardi and Amelung, 2012
Tendürek (Turkey)	InSAR	One sill, ring fault	Bathke et al., 2015
Bárðarbunga (Iceland)	InSAR, seismicity	One sill, ring fault	Riel et al., 2015
	InSAR, GPS, seismicity, etc.	One reservoir, ring fault	Gudmundsson et al., 2016
Wolf (Galápagos)	InSAR	Two sills	Xu et al., 2016
Piton de la Fournaise (Réunion)	GPS	Multiple ellipsoidal sources	Peltier et al., 2009
		One elliptical source, host-rock fracturing	Holohan et al., 2017

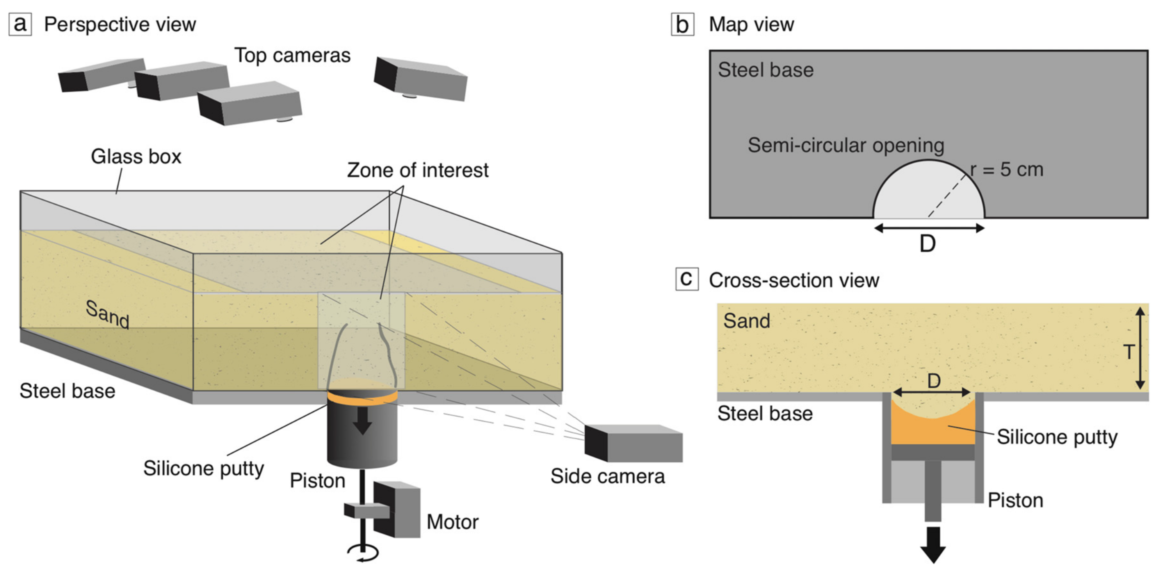

Fig. 2. The analog experiment setup. (a) Perspective view of the sand-filled glass box. The grey-shaded areas indicate the zones of interest where the main deformation occurs. One side camera was placed in front of the box for the subsurface processes while four top cameras were positioned above the box to monitor the surface evolution. (b) Map view of the basal steel plate of the box and the semicircular deformation source. (c) The cross-section view of the setup. A silicone putty (in orange) was placed between the sand-stack and the piston to avoid sand leaking from the box.

cuss the influence of the choice of model on estimating source parameters (e.g., source depths and volume changes) between models that include ring-fault activity and models that consist of multiple reservoirs in homogeneous host rock.

2. Analog experiments of caldera subsidence and collapse

To study caldera collapse in the laboratory, we constructed a glass sandbox analog model with a movable piston at the bottom of the box to simulate host-rock subsidence under magma depressurization. We then used multiple synchronized cameras surrounding the box for deformation field monitoring, which allows us to relate the evolving surface deformation features to the subsurface structures and further analyze the kinematics of the subsidence processes. While the setup of our experiment is comparable to several past analog studies of caldera collapses (e.g., Roche et al., 2000), the novelty here is the simultaneous monitoring of processes at depth (ring faulting) and the resulting surface deformation, using both photogrammetry and digital image offset tracking.

2.1. *Sandbox experiment setup*

The key elements of our analog experimental setup included a transparent glass sandbox and a movable piston controlled by a motor. The size of the box was 30 cm × 30 cm with a maximum depth of 30 cm (Fig. 2a). We loaded the box with horizontal layers of well-sorted crushed silica sand with grain sizes of 40–200 μm (from Valli Granulati). A semicircular opening (10 cm in diameter) at the bottom of the box (Fig. 2b) was connected to a piston, which was driven by a motor stepper and could move vertically with adjustable velocity. To prevent the sand from leaking out from the piston component, a viscous silicone putty was placed between the sand-stack and the piston, which leads to less subsidence near the edges of the piston (Fig. 2c). With this piston setup, we simulated

Table 2
Scaling factors in the analog experiments.

Parameter	Symbol	Model/nature ratio
Brittle crust		
Length	l^*	2×10^{-5}
Density	ρ^*	0.5
Gravity	g^*	1.0
Stress	σ^*	10^{-5}
Cohesion	c^*	10^{-5}

depressurization in a magma reservoir and the resulting crustal subsidence.

To ensure the experiments are comparable to nature, parameters of the analog apparatus should comply with the principle of physical similarity and should be geometrically, kinematically and dynamically scaled to nature. The stress ratio between the analog experiments and nature σ^* can be formulated as: $\sigma^* \approx \rho^* g^* l^*$, where ρ^* is the density ratio, g^* is the gravity ratio, and l^* is the length ratio (Norini and Acocella, 2011; Ruch et al., 2012). To model a 5-km diameter caldera with a 10 cm piston in the experiment, $l^* = l_{model}/l_{nature} \approx 2 \times 10^{-5}$. We take the density of shallow crustal material as 2,600–2,800 kg/m^3 and the density of the quartz sand used in our setup is 1.38 g/cm^3, resulting in a density ratio ρ^* of 0.5. The gravity ratio g^* is 1.0 because our experiments ran under the same gravitational condition as in nature. The apparent cohesion of the crushed silica sand has the same dimension as stress, so the resulting stress ratio σ^* and cohesion ratio c^* are 10^{-5}. In addition, we assumed a linear Mohr-Coulomb failure criterion with an internal friction angle $\phi \approx 40°$ and a natural cohesion $c = 10^7$ Pa (Norini and Acocella, 2011; Ruch et al., 2012) to characterize brittle rock failure in volcanic settings. Considering the cohesion ratio above, the estimated apparent cohesion of the granular material in our experiments should be around 100 Pa, which agrees with our choice of sand that has an apparent cohesion of 12-123 Pa (Galland et al., 2018). For the parameters above, this type of sand thus allows for modeling calderas ranging from about 4 km to over 10 km in diameter (Table 2).

We reproduced several sets of experiments to verify the repeatability of the results of the deformation pattern; we then chose one as representative of the structural evolution to present in this article (Supplement Table S1). Quantitative observations of the experiments were conducted using digital cameras. We aligned five synchronized cameras surrounding the sandbox: one at the side for observing subsurface processes and four on the top for surface changes (Fig. 2a). The side-view camera pointed straight at the cross-section of the setup from a distance of ∼60 cm while the top-view cameras were placed ∼100 cm above the sand-stack with 10°–15° angles between them to ensure sharp images (Galland et al., 2016). All five cameras were standard DSLR (digital single-lens reflex) cameras (four Nikon D3X with Nikkor 55 mm f/2.8 and one D800E with Nikkor 60 mm f/2.8) with a shutter speed of 1/40 and a frame rate of 1 Hz, controlled by a Hähnel Captur infrared remote-control system that synchronously activated five receivers installed on the cameras.

Application of the structure-from-motion technique allows to retrieve quantitative surface deformation (Galland et al., 2016). We used a stand-alone spatial photogrammetry software (Agisoft Photoscan) and our top-view photographs to construct a series of digital elevation models (DEMs) of the evolving topographic surface. Based on a detailed point cloud derived from each set of synchronized images, a high-resolution DEM was produced after defining ground control points and the scale between the model and the images. The resolution of the DEMs corresponds to the pixel size of the captured images, i.e. ∼0.11 mm/pix using these 24.5-megapixel cameras placed at one meter above the sand-stack surface. The resulting multi-temporal DEM provide a detailed time-series of the evolving surface topography.

High-resolution digital image correlation is often applied to track the evolving displacement field of scaled analog experiments. We used PIVlab (Thielicke and Stamhuis, 2014), an open-source image correlation software running in Matlab, to cross-correlate temporally successive image pairs captured with both the top-view and the side-view cameras. Based on the referenced scaling, image pixel offsets were then converted to displacement, velocity and vortex fields (Burchardt and Walter, 2010; Ruch et al., 2012) of the granular particles through time. The vortex field reflects the shear strain in the sand and here we interpret the observed shear strain localizations as “faulting”, for convenience.

2.2. Structural characteristics and evolution

The onset of piston sinking drew the sand-stack downward and deformed the ground surface. Meanwhile, shear strain localizations initiated from the edge of the piston in the subsurface. They developed upward and eventually reached the surface and magnified the ground displacements throughout the experiments. We use reverse and normal ring faulting (RF and NF) to describe the sense of localized shear strain in the analog model experiments. At the surface, we use “near field” and “far field” for the areas inside and outside the subsiding source boundary (i.e. within the 10 cm source diameter), respectively. The overall subsidence evolution in the experiments could be separated into an earlier downsag stage and a later collapse stage, based on the observed deformation features and the onset of surface rupturing, which started at ∼4.8 mm of subsidence (i.e., after 90–100 s at steady piston rate of 0.04 mm/s).

During the downsag stage, compressive ridges formed around the center of the subsidence bowl (map view; inset Fig. 3a). This compressive regime (negative dilatational strain; the red area) was caused by movements of buried reverse ring faults (RFs) located below the compressive ridges (section view; inset Fig. 3b), which grew with increasing subsidence. As expected, the deformation in the near field is stronger and more localized than in the far field, with the topographic changes dominated by concentrated subsidence, while further away the topographic changes are featured by steady subsidence. In addition to the RFs, extensional regime and fractures also formed at the surface (positive dilatational strain; the blue area in inset Fig. 3a) due to gravitational instability of the slopes formed by the buried RFs.

In the collapse stage, normal faults (NFs) started to nucleate from the surface extensional fractures which coincides with the boundary of the underlying piston (the black, circular dashed lines in Fig. 3c). As the collapse evolved, the circumferential NFs developed and further delineated a caldera structure (Fig. 3d). The near-field subsidence accelerated with increasing RF and NF activity, while the far-field subsidence remained stable without progressing much further. Different subsiding rates between the two fields led to prominent topographic changes across the surface. Snapshots of north-south and east-west surface profiles (Fig. 3 e, f) show how the ground surface progressed from the downsag stage (40, 60, 90 s) to the collapse stage (110, 130, 160 s). The former was mainly affected by broad and smooth subsidence, while the latter was dominated by concentrated subsidence in the near field. Most of the far-field subsidence occurred during the downsag stage, so the far-field topography remained mostly stable after ∼90 s.

2.3. Surface deformation

Vertical and horizontal surface displacements were retrieved from the DEM time-series of the evolving ground surface and from the image correlation results of successive top-view photographs,

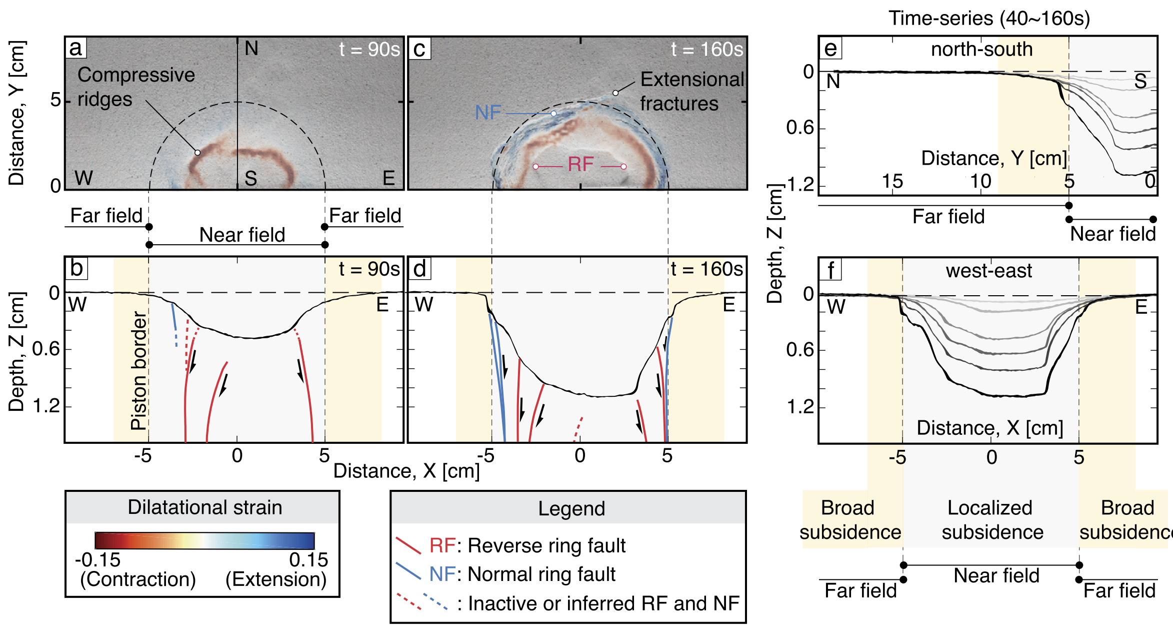

Fig. 3. Surface and subsurface structures of laboratory caldera collapse. (a) The downsag stage of the subsidence features a gentle central depression and compressive ridges. (b) Subsurface mapping of ring faults at depth late in the downsag stage at $t = 90$ s. Reverse faults (RF; in red) have almost progressed to the surface and normal faults (NF; in blue) have just started to form. Concentrated and localized subsidence can be seen in the near field (in grey) and smooth subsidence in the far field (in yellow). (c) Surface structures during the collapse stage after the ring faults rupture the surface at 90–100 s. (d) Subsurface mapping late in the collapse stage at $t = 160$ s where both outward-dipping RFs and inward-dipping NFs are active. (e) Temporal evolution of N-S and (f) E-W topographic profiles (plotted at 40, 60, 90, 110, 130, and 160 s) show that the overall subsidence is localized primarily in the near field.

respectively. For better comparison to InSAR observations, and to reveal more details of the deformation pattern, we display the resulting surface displacements using wrapped deformation maps with InSAR-like fringe patterns, with one fringe corresponding to 0.4 mm displacement in the line-of-sight (LOS) direction. We used a LOS vector typical of an ascending-track satellite SAR image (e.g. ALOS-2), acquired from an orbit with a heading of N345°E and an incidence angle of 36° (the top right panel of Fig. 4).

From the time-series of surface displacements, we find that a broad subsidence area was formed at the beginning of the downsag stage. This initial subsidence came with the onset of the piston sinking and is revealed by the smooth fringe pattern covering both the near and far fields with clear fringe spacing (Fig. 4a). The broad subsidence bowl steadily grew throughout the experiment. Localized subsidence in the near field, however, only started to occur at the end of the downsag stage when the ring faults reached the surface. As the ring faults further developed with increasing activity, the caldera surface progressively collapsed. The collapse stage is characterized by intense near-field subsidence as illustrated by localized fringe patterns and small fringe spacing (Fig. 4c), resulting in sharp and steep topography.

Further analysis of the subsidence time-series shows that the magnitude of the near-field and the far-field subsidence was similar (about one fringe) at early stages of the experiments (Fig. 4a). Defining the subsidence difference between the near and the far fields as ΔS = [near-field subsidence] − [far-field subsidence], we found that ΔS is close to zero at $t = 40$ s, with a maximum subsidence at the caldera center of about 0.8 mm. Then, the subsidence in the near field started to increase faster than in the far field, with $\Delta S \approx 0.6$ mm at $t = 60$ s, with a maximum subsidence of about 1.9 mm. At $t = 90$ s, the steady far-field subsidence and the rapid near-field subsidence yielded a larger ΔS of ~3.0 mm and a maximum subsidence of ~4.8 mm. The different subsidence rates between the near and the far field (at ~90 s) resulted in distinctive features of the fringe pattern, with a broad subsidence overlapped by a localized subsidence (also Fig. 3e, f).

In the collapse stage, the difference between the near-field and the far-field subsidence continued to increase (Fig. 4c) with ΔS reaching ~4.0 mm at $t = 110$ s and the maximum subsidence at the caldera center ~6.4 mm. At $t = 130$ s and 160 s, ΔS increased to ~6.0 mm and ~6.6 mm, with the maximum subsidence of ~8.5 mm and ~11.2 mm, respectively. The evolution of ΔS shows the dominant role of the ring faulting in explaining most of the surface deformation. In addition, the perimeter of the concentrated fringe pattern demonstrates the close relationship between the ring-fault location and the extent of the localized subsidence.

A piston displacement of ~4.0 mm (when the ring fault reached the surface) scales to ~200 m subsidence and magma volume loss of ~3.9 km^3 for a 5-km caldera, which is comparable to natural cases. For example, the subsidence of the caldera floor during the 2014–15 Bárðarbunga event was 60 m and the volume loss was ~2 km^3 for a 10-km caldera (Gudmundsson et al., 2016). The Miyakejima collapse in 2000 produced a subsidence of ~450 m during a ~1 km^3 volume withdrawal from a 1.6 km wide caldera (Geshi et al., 2002). Finally, the 5 km wide Kilauea caldera subsided from 150 m to 550 m in 2018 and produced ~1 km^3 of lava (Neal et al., 2018).

2.4. Structural processes in cross-section

The evolution of the subsurface structures in the experiments is closely related to the observed surface deformation. The downsag stage is characterized by the development of the buried reverse faulting and smooth deformation of the sand-stack, while the collapse stage is featured by the reverse faulting reaching the surface, the onset of normal faulting, and the localized near-field subsidence. Here we present section-view photographs overlain with the rotational strain of the in-depth material calculated using the image correlation technique (Fig. 4b, d), with clockwise rotational strain in red and counterclockwise in blue.

The image correlation analysis shows that the RFs initiated during the downsag stage at $t = 40$ s from the periphery of the piston (red and blue; Fig. 4b) are due to accumulating shear stress local-

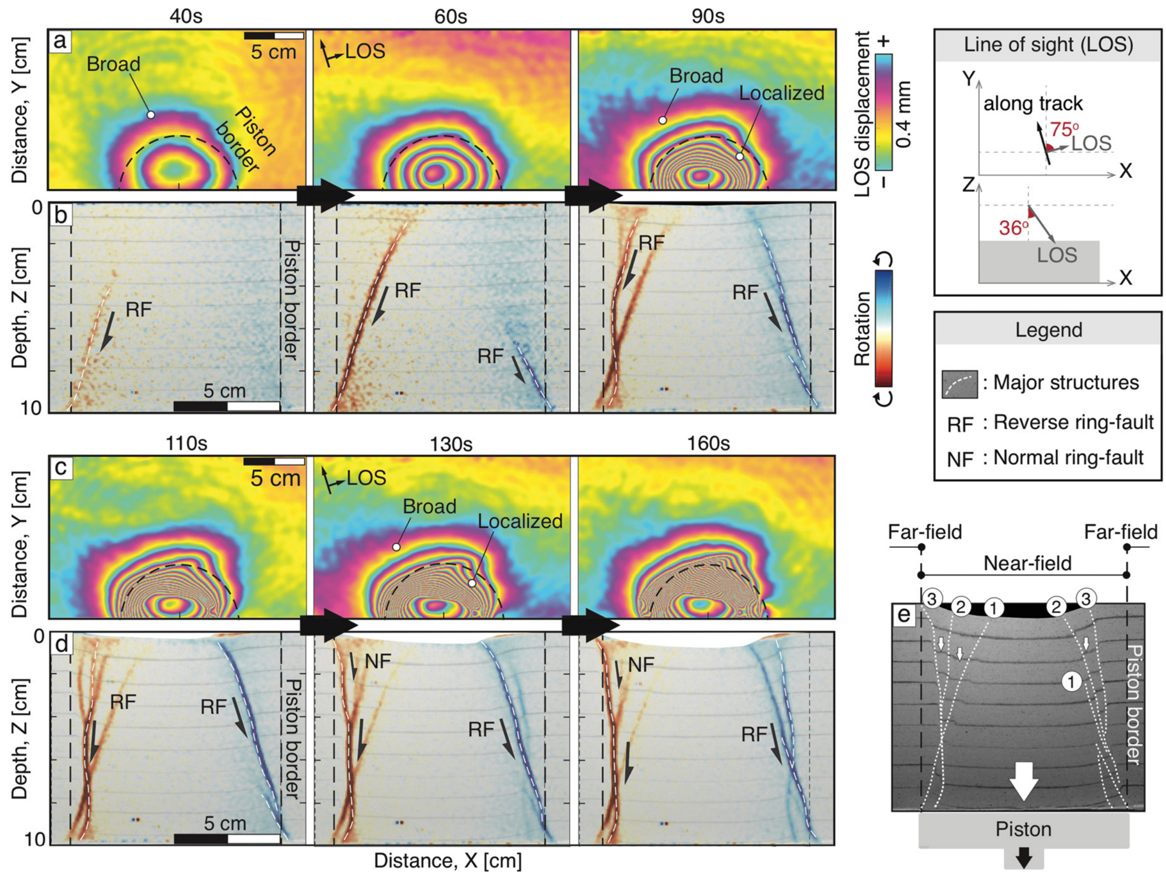

Fig. 4. Subsidence evolution derived from surface and side-view image processing. (a) Wrapped surface deformation at different times (at $t = 40$ s, $t = 60$ s, and $t = 90$ s) during the downsag stage showing cumulative displacements from $t = 0$ s. The crossed arrow indicates the ascending LOS vector used to produce these interferogram-like deformation maps (for further information, see top right panel). (b) Cross-sectional view photos overlain with the rotation field (shear strain concentration), revealing the location of ring faults in the subsurface. Arrows indicate the sense of motion. (c) Surface deformation and (d) the rotational field at different times (at $t = 110$ s, $t = 130$ s, and $t = 160$ s) during the collapse stage. (e) The major ring faults developed from the innermost outward-dipping reverse faults to the outermost subvertical and inward-dipping normal faults.

ization. The upper edges of the ring faults (hereafter called "fault tips") at this stage were located at ∼4 cm below the surface. With increasing subsidence and more intense shear strain in the sand, the RFs propagated further upward with the fault tips at ∼1 cm depth at $t = 60$ s. At the end of the downsag stage ($t = 90$ s), both sides of the outward dipping RFs enclosing the central subsiding volume reached the surface and higher dip angle RF branches developed.

During the collapse stage, the central subsidence gradually developed into a semicircular caldera collapse bordered by the normal faulting (Fig. 4d). At $t = 110$ s, the numerous branches of subvertical RFs grew in succession around the primary RFs, enhancing the complexity of the fault system. At $t = 130$ s, an inward dipping NF developed, which originated from an open fracture at the surface on the left. The NF further developed due to the instability of the hanging-wall block of the RFs, propagating downward and merging with the subvertical RFs (see also Fig. 3b, d). At $t = 160$ s, the development of the NFs had enlarged the subsiding area surrounding the near field, together with the subvertical RFs merging below, yielding an efficient piston-like collapse (160 s of Fig. 4d).

3. Boundary element modeling

To further analyze the deformation patterns caused by a depleting magma reservoir and an active ring fault, we carried out numerical simulations based on the boundary element method (BEM). The BEM is an efficient technique as only source boundaries need to be discretized and thus, it is often applied in modeling of dike intrusions or earthquake fault slip in an elastic half-space. The source boundaries can be complex, although in our case we approximate a depleting magma body with a closing sill-like horizontal crack (Fialko et al., 2001a) and the ring faulting by a conical fault plane slipping in the dip-direction (Beauducel et al., 2004; Bathke et al., 2015). We modeled the subsidence from the initial downsag to the later collapse by running several cases composed of different sill and ring-fault configurations.

3.1. Boundary element method setup

We used a sill-like horizontal magma reservoir that interacts with a conical ring fault above it (Fig. 5). We let sill closure represent volume decrease in the sill-like magma body (Amelung et al., 2000; Bagnardi and Amelung, 2012) and the ring fault responds to the depressurization by fault slip (Bathke et al., 2015). The geometry of the two sources was constructed using two sets of meshes composed of triangular dislocations (Nikkhoo and Walter, 2015). Given appropriate boundary conditions (tractions) on each triangular dislocation as perturbations of an initial state of stress, we calculated the resulting displacements on all the source dislocations by using the least squares method. In this linear system, we further added up all the surface displacements caused by each dislocation, applying the principle of superposition in order to get the total displacement field at the surface of the elastic half-space induced by both the ring faulting and the sill closure (Segall, 2010).

The sill model was designed as a disk with a diameter of 2.0 km and was placed at 4.08 km depth. Based on the analy-

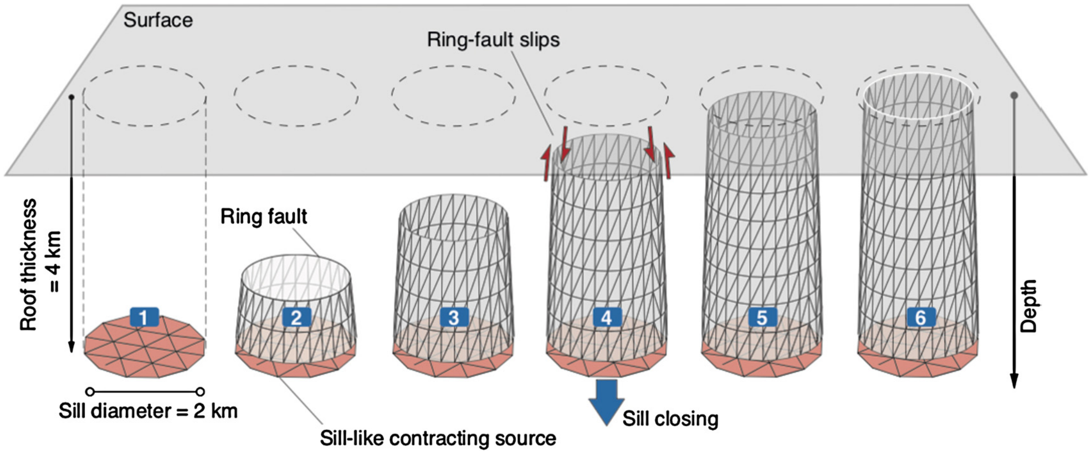

Fig. 5. The model setup for BEM calculations. The deformation sources consist of a horizontal contracting sill and a ring fault, discretized into triangular dislocations. Circular dashed lines indicate the projected sill-like source border at the surface. The sill diameter is 2 km and it is placed at ∼4 km depth, leading to a "thickness of roof"/"diameter of source" ratio T/D = 2.0. Different BEM setups from 1 to 6 are implemented with progressively shallower ring fault to resemble possible upward propagation of the ring faulting.

sis of caldera geometries related to source dimensions, our collapse model has a thickness to diameter ratio $T/D \cong 2$, representing a thick-roof geometrical collapse setting (Roche et al., 2001; Geyer et al., 2006). Thick-roof collapses are featured by reverse faulting on relatively steep outward-dipping ring faults (Holohan et al., 2011), which we approximated by the steep ring-fault geometry of our BEM source setups. This steep ring-fault geometry has also been revealed by seismicity at Bárðarbunga Volcano, for example (Ekström, 1994; Nettles and Ekström, 1998), and has been seen in previous experimental studies (Roche et al., 2001; Acocella, 2007; Ruch et al., 2012) and in our analog experiments. We parametrized the geometry of the ring fault from two circles at different depths, representing the upper edge (diameter of 1.8 km) and lower edge (diameter of 2.0 km) of the ring fault. The fault plane was then linearly interpolated between these two circles. We kept the lower edge of the ring fault at 4.0 km depth and simulated upward migration of the ring fault by moving the upper edge of the ring fault in consecutive runs closer towards the surface (setup 1–6 in Fig. 5).

We took the fault plane as frictionless while the sill, as the active deformation source, was given uniform negative tensile stress to model the depletion within a reservoir. This simulates a sill closure under a specific stress drop with the ring fault responding with slip in the dip-direction. The subsurface medium otherwise was considered as isotropic, linearly elastic and homogeneous, and we considered a shallow crust setting with a Poisson's ratio of $\nu = 0.25$ and Lame's constants of $\lambda = \mu = 33$ GPa (Bathke et al., 2015). The uniform tensile stress boundary condition on the sill was set to −33 MPa (negative indicates compression) to generate a maximum of 1 m sill closure in setup 1. Similarly, for setups 2 to 6, we adjusted the sill stress to yield the same maximum closure of the sill.

Although using a frictionless fault at the depth of the magma reservoir where the temperature is high might be acceptable, at shallower depths a fault with some strength seems more plausible. Frictional fault slip would not occur unless the change in stress is larger than the strength on the fault. However, including friction into the BEM setup is beyond the scope of this article (Maerten et al., 2010) as here we are primarily focused on investigating the relationship between deformation patterns at the surface and active ring-fault structure at depth.

3.2. BEM results

We show the resulting surface displacement fields of several BEM calculations that together approximate the temporal evolution of the ring-faulting process from the initial downsag stage to the later mature collapse stage (Fig. 6). Our results show that for the same sill location and closure settings, the different depths of the upper edge of the ring fault generate distinctive subsidence patterns at the surface.

Depressurization within a single reservoir placed at 4.08 km depth without any ring faulting (setup 1) generates a broad and smooth subsidence bowl (shown by fringe patterns with large spacing) at the surface. The broad subsidence bowl has a maximum vertical displacement of 7.0 cm and clear subsidence up to 5 km away from the center of deformation (Fig. 6a). Setups 2 and 3 were implemented with deep ring faults whose upper fault edges are at 3.0 km and 2.0 km below the surface, respectively. These setups produce up to 7.9 and 10.8 cm of maximum subsidence respectively and already show focusing of displacements in the near field (Fig. 6b, c). Setups 4 and 5 have the fault tips at only 1.0 km and 0.3 km depth producing both increasingly more localized subsidence and stronger vertical displacements in the middle (Fig. 6d–e), with maximum subsidence of 18.0 cm and 32.4 cm, respectively. Finally, as the ring fault reaches the surface (setup 6), a piston-like collapse with a maximum subsidence of 47.4 cm causes deformation fringe aliasing (Fig. 6f). While the near-field surface displacements increase, the average far-field displacements decrease from 2.9 cm in setup 1 to 1.8 cm in setup 6. The deformation characteristics and contributions of ring faulting on one hand and sill depletion on the other hand are separated and shown for setup 4 in Fig. 6g. The displacements due to ring faulting are concentrated and are confined mostly in the near field (red curve; Fig. 6g), whereas the sill closure produces a broad and smooth subsidence bowl at the surface (blue curve). Therefore, the sharp and concentrated near-field subsidence overlain on a broad subsidence bowl, which has been observed at several volcanoes, can thus be produced by a single deep sill-like deflating source and shallow ring-fault movements.

The profiles of vertical displacement in Fig. 6h show the gradual evolution of the caldera subsidence from the initial sill deformation of setup 1 to the stronger and more concentrated piston-like collapse in setup 6. The early profiles of setups 1–4 with deeper ring-fault tips demonstrate broad and rather smooth subsidence due to the subtle contributions of the ring faulting (Fig. 6a–d). These setups resemble the downsag stage of the caldera subsidence in our analog experiments. Setups 5–6, with shallower ring-fault tips, tend to have stronger and more localized displacements because the ring faulting is approaching the surface and its effects are more clearly seen on the surface (Fig. 6e, f). These setups are

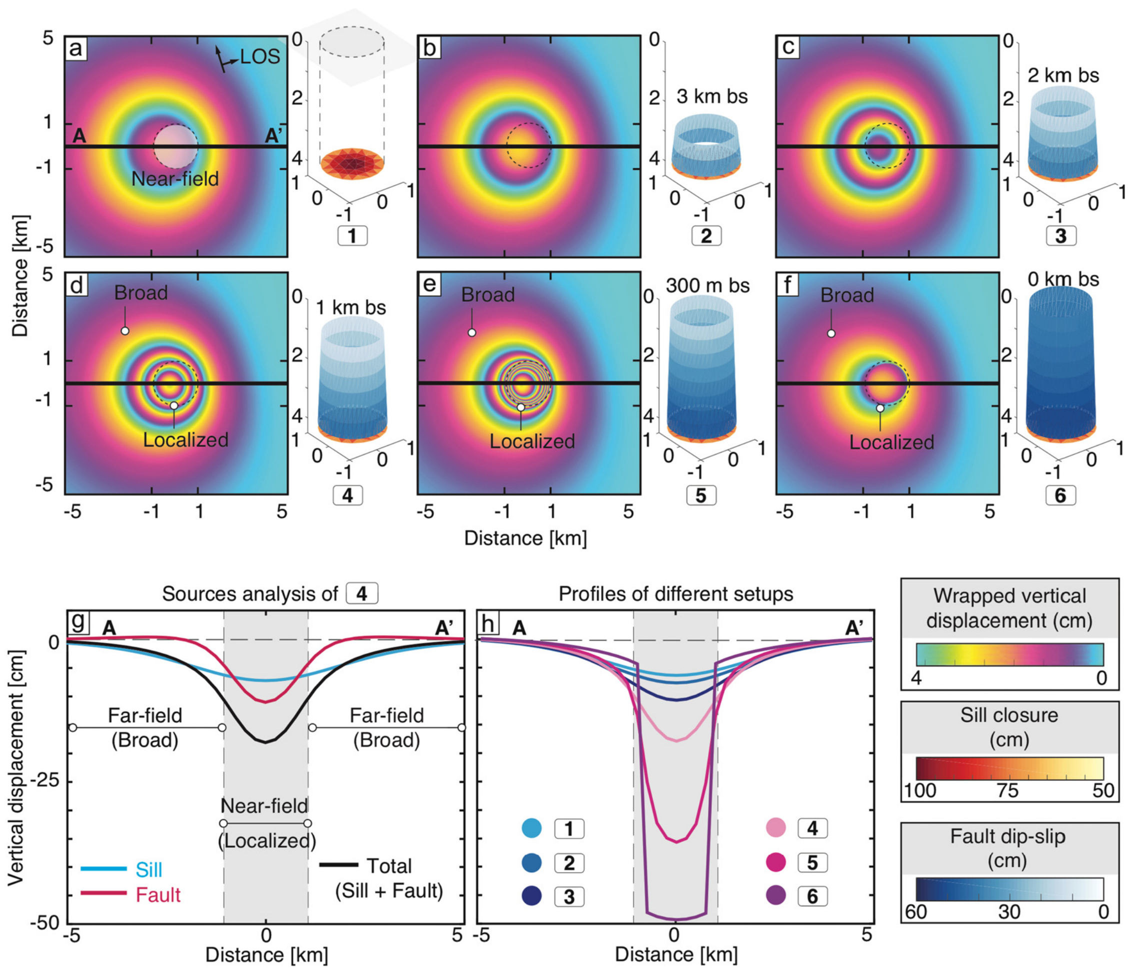

Fig. 6. Surface displacements from the BEM calculations. (a–f) Surface deformation illustrated as wrapped fringe maps (ascending LOS projections; 4 cm per fringe) for the six different BEM setups, showing increasingly focused near-field displacements as the ring faulting becomes shallower. (g) Vertical displacement profiles for BEM setup 4 showing the displacement contributions from the sill closure and the ring faulting separately. (h) Vertical surface displacement profiles for the six BEM setups.

therefore more like the collapse stage of our analog experiments. As the volume change of the sill remained almost identical in all these setups, the surface displacement differences are primarily controlled by the depth extent and amount of the ring faulting.

The BEM calculations reported here represent a thick-roof geometrical collapse setting with $T/D = 2$ (Holohan et al., 2011). We also carried out simulations under an intermediate roof collapse setting ($T/D = 1$) by using a sill with a diameter of 4.0 km at the same depth as before, interacting with a ring fault with its lower diameter of 4.0 km and upper diameter of 3.8 km. This change to the sill and fault geometry results in different surface displacement amplitudes, slip values on the ring fault, and the required closing traction of the sill. However, the overall deformation trends and implications are the same as for $T/D = 2$ (see supplementary materials Fig. S1).

3.3. Two-sill models

While two or more models may fit geodetic data at a volcano equally well, choosing an inappropriate model may lead to incorrect interpretations about subsurface processes. To demonstrate this issue, we use an alternative model composed of two sills at two different depths to explain displacement profiles produced by our BEM setups consisting of a single deflating sill and ring faulting, as shown in Fig. 6. For the two-sill models, we fixed the lower sill at 4.08 km depth, with a diameter of 2 km and a volume change of 2.6×10^6 m^3. We then tuned the upper sill parameters (diameter, depth, and volume change) such that the resulting surface displacements approximately matched the displacements produced by the BEM models (Fig. 7a–d). As the tip of the ring fault in the BEM setups becomes shallower, from 3.0 km to 1 km and then to 0.3 km, the resulting displacement profiles have more localized subsidence. To adequately fit these displacement profiles, the upper sill of the two-sill model has to be progressively shifted from 3.0 km to 0.9 km and then to 0.42 km, respectively (Fig. 7a–c). The diameter of the upper sill also changes from 2.0 km to 1.8 km. When the ring faulting reaches the surface, leading to a collapse and strong surface displacement discontinuities across the ring fault, the two-sill model does not match the BEM displacement profile well (Fig. 7d). In general, the estimated depth of the sill migrates toward the surface along with the progressive upward development of the BEM ring fault. Similar upward migration of the estimated magma reservoir as subsidence increases was also pointed out by Holohan et al. (2017) using discrete element method simulations with host-rock fracturing. Together, these lines of evidence indicate that the true depths of pressure sources under calderas are usually underestimated and they may be impossible to constrain from geodetic data alone in the presence of ring faulting.

Another issue is the estimated magma volume change. For the BEM models, the single-sill volume change in each case is roughly 2.6×10^6 m^3 (blue bars in Fig. 7e), despite the different ring-fault geometries. While the lower-sill volume change in the two-sill case was set to be identical to the BEM sill volume change (roughly 2.6×10^6 m^3), the upper-sill volume change needs to increase from

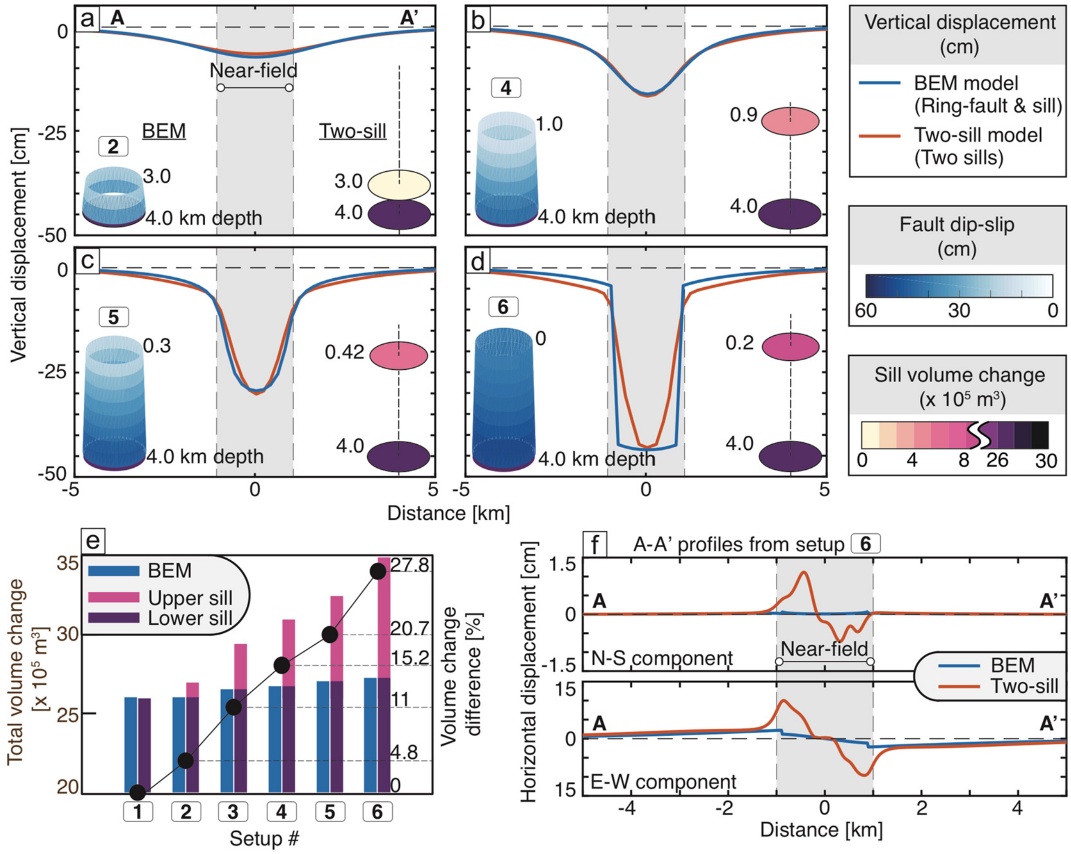

Fig. 7. Comparison between the vertical displacement profiles from the BEM setups and models with two depleting sills. (a–d) The superimposed surface displacements from the BEM setups can be reproduced approximately by two-sill models. For BEM setups with shallower ring faulting, a shallower upper sill is required in the two-sill model with a larger volume decrease. (e) The volume change of each BEM setup and of each corresponding two-sill model. (f) Horizontal displacements along the A-A' profile help to discriminate between the two source models.

1.3×10^5 to 7.6×10^5 m^3 to match the BEM displacement profiles (Fig. 7e). As a result, the estimated total volume change of the two-sill models increases significantly, going from being identical to the BEM volume change without ring faulting (setup 1) to being ∼20% larger when matching the BEM displacement profile with a ring-faulting tip at 0.3 km (setup 5). This indicates that in cases where a single magma reservoir is triggering ring faulting, one would overestimate the volume change by assuming a two-sill model, in particular if the active ring faulting is close to the surface.

4. Discussion

We have utilized two complementary methods to improve understanding of the subsurface processes that may be responsible for the observed volcanic deformation consisting of both volcano-wide smooth deflation and localized caldera subsidence (Fig. 1). Below, we will relate our results to cases in nature and then discuss some challenges in volcano geodesy concerning the estimation of deformation sources using geodetic data.

The overlapping displacement patterns observed at Wolf volcano and at Fernandina have been explained by pressure changes within two magma reservoirs at different depths (Chadwick et al., 2011; Bagnardi and Amelung, 2012; Xu et al., 2016). These results suggest that the localized subsidence inside the caldera may be linked to the shallower reservoir deflation while the broader deformation to the deeper reservoir. In contrast to these interpretations that include more than one reservoir, we have demonstrated by analog and BEM modeling, that overlapping deformation patterns may also be due to deflation of a single reservoir in combination with ring-fault activity.

Comparing the results of the analog modeling with the case studies mentioned above may seem questionable. The analog experiments model a full caldera evolution including a collapse and formation of ring-fault structures. The case studies, on the other hand, represent only moderate subsidence events at already developed calderas that structurally are well beyond the downsag stage. However, moderate depressurization of a caldera reservoir would not cause further caldera collapse with surface faulting, but rather begin by reactivating ring faulting at depth with subtle subsidence at the surface, similar to the downsag stage of the analog experiments. This said, however, we also tried modeling reactivation of pre-existing ring faults in the analog experiments, by stopping the piston for a while and then restarting its withdrawal, but it turned out to be challenging and provided limited results (Supplement section 1.2). Another issue with the analog modeling includes boundary effects, such as friction of the glass pane, which slightly offsets the deformation pattern but does not appear to significantly affect the overall kinematics. We thus think the benefit of having a cross-sectional view of the ring-fault activity at depth at the same time as the resulting deformation at the surface outweighs this design limitation. A further simplification is that the models do not include topography. To assess topographical effects, we carried out an experiment with a conical volcanic edifice (Supplement section 1.3) and similar complex deformation features were observed, indicating that topographical influence is limited, at least in presence of gentle topography.

In the BEM calculations, we used a single outward dipping ring fault with a constant dip-angle and without any fault branches. This setup simplifies what we observed in our analog experiments and what has been seen in other studies (Fig. 4 and Fig. 5;

Roche et al., 2001; Acocella, 2007; Holohan et al., 2011) where mature ring faults have been found to be composed of a major outward dipping reverse fault as well as of an inward dipping normal fault. However, the architecture of the ring-fault system depends not only on the geometrical setting (i.e. reservoir's shape, T/D ratio, etc.; Roche et al., 2001; Holohan et al., 2011), but also on mechanical factors (e.g. rock strength; Holohan et al., 2011). In addition, development of ring-fault branches can be complicated and somewhat unpredictable (stochastic), as shown in our analog experiments, and is thus not always reproducible. Therefore, considering these possible fault segments and geometries in the BEM calculations would probably not add valuable information. Furthermore, even if inward dipping normal ring faults appear at the later collapse stages in analog experiments, the majority of the surface subsidence is likely related to displacement on the outward dipping reverse ring fault. Therefore, we focused on the primary structure and only used a single outward dipping ring fault in the BEM calculations.

Geodetic data play a key role in constraining parameters of models that describe possible deformation sources at active volcanoes and the model parameters provide useful information about underlying magma bodies, e.g., their dimensions, location and volume change (Dzurisin, 2003; Poland et al., 2006). However, more than one model can usually be applied to explain the same set of observations. Therefore, parameters of deformation sources can be difficult to constrain uniquely, particularly when the host-rock contains heterogeneities, such as dike intrusions, faults, or layering (Trasatti et al., 2003; Manconi et al., 2007; Bagnardi and Amelung, 2012). As ring faults are probably the most obvious structural inhomogeneities in calderas, we conclude that the superimposed displacements observed by satellite interferograms at volcanoes such as Wolf (Xu et al., 2016) and Fernandina (Chadwick et al., 2011; Bagnardi and Amelung, 2012) are most likely a consequence of changes within a single deep magma reservoir interacting with subsurface ring faulting.

Using two sill-like pressure sources to model observed displacements, that are in fact caused by a single deflating sill interacting with ring faulting, will lead to considerable underestimation of the magma source depth and overestimation of the volume change. In addition, when the surface deformation is intense, this choice of model can lead to unrealistic volume changes and very shallow depth estimates, as has been recognized at Campi Flegrei in Italy (De Natale et al., 1991; Trasatti et al., 2005), Kilauea in Hawaii (Davis, 1986; Dieterich and Decker, 1975) and Rabaul in Papua New Guinea (De Natale et al., 1997; Saunders, 2001). The localized deformation observed in these cases was considered to be beyond the elastic limit, particularly at localized inhomogeneities, such as at caldera ring faults. Therefore, mechanically weak ring-fault systems and ring-fault slip that enhance caldera deformation are likely to be misinterpreted as near-surface magma reservoirs.

As described above, mechanical explanations for observed volcano deformation are not unique (Dieterich and Decker, 1975; Fialko et al., 2001b) and it can be difficult to distinguish between different possible deformation sources (e.g. two-sill models versus BEM models, see Fig. 7). In the above comparison, we only considered vertical displacement profiles, but including horizontal displacement components can sometimes help to differentiate between different source types (Fialko et al., 2001a; Yun et al., 2006). The two-sill model, for example, generates stronger horizontal displacements than the corresponding BEM model (Fig. 7f). In practice, we often only have InSAR line-of-sight measurements of volcanic deformation, which are usually less sensitive to horizontal displacements than to vertical displacements. We also often lack images from the opposite-looking InSAR satellite track that are needed to separate between vertical and ∼east-west horizontal displacements. When available, GPS data can help as they provide

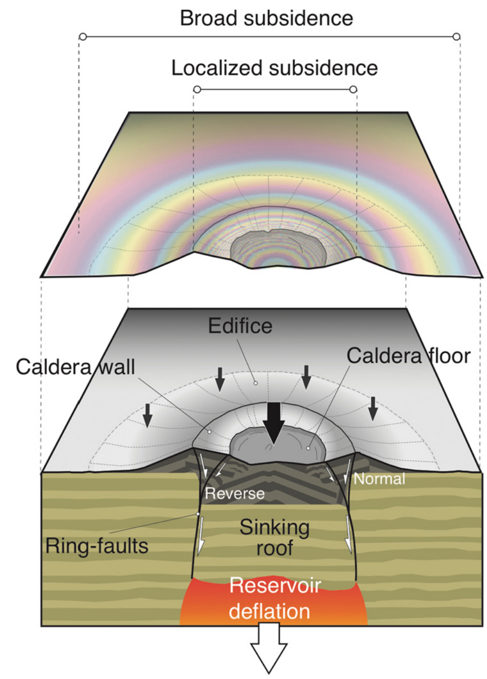

Fig. 8. Schematic figure of caldera subsidence due to magma reservoir deflation and ring-fault activity. We propose that the broad and smooth subsidence affecting entire volcanic edifices and the concentrated subsidence confined within calderas are caused by the deflation of a single deep magma reservoir and ring faulting (the dimensions are not drawn to scale).

3D displacement information at locations where GPS instruments are installed. In summary, these challenges in volcano geodesy highlight the importance of using other data, e.g., seismic data and seismic imaging results (when available), and mapped structural information (Nettles and Ekström, 1998; Aoki et al., 2013; Gudmundsson et al., 2016), as well as geochemical and petrological analysis of erupted lavas. Together, such interdisciplinary data should be integrated to yield more realistic subsurface models and to improve images of the active subsurface volcanic structures.

5. Conclusions

Observed surface deformation patterns at several subsiding calderas, consisting of both localized and broad subsidence, have usually been modeled using two magma reservoirs at two different depths. Such models ignore caldera ring fault structures and possible fault slip, which may be driven by moderate deflation of the underlying magma reservoir, thus localizing surface deformation within calderas. Combining analog experiments and BEM modeling of caldera deformation processes, we have shown that subsurface ring faulting associated with deflation within a single reservoir offers an alternative and more plausible explanation for the observed overlapping deformation patterns, compared to models consisting of two or more reservoirs (Fig. 8). In particular, the two-reservoir model requires the upper source to migrate towards the surface to fit deformation that over time becomes increasingly localized, a temporal pattern that is more realistically explained with progressively shallower ring faulting caused by increasing reservoir deflation.

Possible ring faulting under deforming calderas leads to difficulties in determining parameters of subsurface magma reservoirs. Ignoring ring-fault activity may not only lead to inappropriate model choices consisting of multiple magma reservoirs but also to incorrect estimations of the subsurface magma volume changes. In addition, trade-offs between ring-fault activity and magma reservoir characteristics make it challenging to accurately determine the magma reservoir depth from geodetic data alone. These limitations of volcano geodesy show the importance of integrating additional data into the model setup and interpretation, including locations of ring-fault related earthquakes and mapped structures, when studying unrests and activity at calderas.

Acknowledgements

We thank Prof. Sigurdur Thoroddsen, Dr. Nadia Kouraytem, Dr. Andres A. Aguirre-Pablo, and Aditya Jetly in the High-Speed Fluids Imaging Laboratory at King Abdullah University of Science and Technology (KAUST) for providing camera equipment and laboratory facilities for our analog experiments. The granular material used in the analog experiments was provided by Dr. Daniele Trippanera (Roma Tre University, now at KAUST). We also thank Mehdi Nikkhoo for fruitfull discussions as well as Yosuke Aoki and one anonymous reviewer that helped to improve the quality of the manuscript. The research reported in this publication was supported by KAUST, award number BAS/1/1353-01-01.

Appendix A. Supplementary material

Supplementary material related to this article can be found online at https://doi.org/10.1016/j.epsl.2019.115784.

References

Acocella, V., 2007. Understanding caldera structure and development: an overview of analogue models compared to natural calderas. Earth-Sci. Rev. 85, 125–160. https://doi.org/10.1016/j.earscirev.2007.08.004.

Amelung, F., Jónsson, S., Zebker, H., Segall, P., 2000. Widespread uplift and 'trapdoor' faulting on Galápagos volcanoes observed with radar interferometry. Nature 407, 993–996. https://doi.org/10.1038/35039604.

Aoki, Y., Takeo, M., Ohminato, T., Nagaoka, Y., Nishida, K., 2013. Magma pathway and its structural controls of Asama Volcano, Japan. Geol. Soc. (Lond.) Spec. Publ. 380, 67–84. https://doi.org/10.1144/SP380.6.

Bagnardi, M., Amelung, F., 2012. Space-geodetic evidence for multiple magma reservoirs and subvolcanic lateral intrusions at Fernandina Volcano, Galápagos Islands. J. Geophys. Res. B, Solid Earth Planets 117. https://doi.org/10.1029/2012JB009465.

Bathke, H., Nikkhoo, M., Holohan, E.P., Walter, T.R., 2015. Insights into the 3D architecture of an active caldera ring-fault at Tendürek volcano through modeling of geodetic data. Earth Planet. Sci. Lett. 422, 157–168. https://doi.org/10.1016/j.epsl.2015.03.041.

Beauducel, F., De Natale, G., Obrizzo, F., Pingue, F., 2004. 3-D modelling of Campi Flegrei ground deformations: role of Caldera boundary discontinuities. Pure Appl. Geophys. 161, 1329–1344. https://doi.org/10.1007/s00024-004-2507-4.

Biggs, J., Ebmeier, S.K., Aspinall, W.P., Lu, Z., Pritchard, M.E., Sparks, R.S.J., Mather, T.A., 2014. Global link between deformation and volcanic eruption quantified by satellite imagery. Nat. Commun. 5, 3471. https://doi.org/10.1038/ncomms4471.

Burchardt, S., Walter, T.R., 2010. Propagation, linkage, and interaction of caldera ring-faults: comparison between analogue experiments and caldera collapse at Miyakejima, Japan, in 2000. Bull. Volcanol. 72, 297–308. https://doi.org/10.1007/s00445-009-0321-7.

Chadwick, W.W., Jónsson, S., Geist, D.J., Poland, M., Johnson, D.J., Batt, S., Harpp, K.S., Ruiz, A., 2011. The May 2005 eruption of Fernandina volcano, Galápagos: the first circumferential dike intrusion observed by GPS and InSAR. Bull. Volcanol. 73, 679–697. https://doi.org/10.1007/s00445-010-0433-0.

Cole, J.W., Milner, D.M., Spinks, K.D., 2005. Calderas and caldera structures: a review. Earth-Sci. Rev. https://doi.org/10.1016/j.earscirev.2004.06.004.

Davis, P.M., 1986. Surface deformation due to inflation of an arbitrarily oriented triaxial ellipsoidal cavity in an elastic half-space, with reference to Kilauea volcano, Hawaii. J. Geophys. Res. 91, 7429. https://doi.org/10.1029/JB091iB07p07429.

De Natale, G., Petrazzuoli, S.M., Pingue, F., 1997. The effect of collapse structures on ground deformations in calderas. Geophys. Res. Lett. 24, 1555–1558. https://doi.org/10.1029/97GL01600.

De Natale, G., Pingue, F., Allard, P., Zollo, A., 1991. Geophysical and geochemical modelling of the 1982-1984 unrest phenomena at Campi Flegrei caldera (southern Italy). J. Volcanol. Geotherm. Res. 48, 199–222. https://doi.org/10.1016/0377-0273(91)90043-Y.

Dieterich, J.H., Decker, R.W., 1975. Finite element modeling of surface deformation associated with volcanism. J. Geophys. Res. 80, 4094–4102. https://doi.org/10.1029/JB080i029p04094.

Dzurisin, D., 2003. A comprehensive approach to monitoring volcano deformation as a window on the eruption cycle. Rev. Geophys. 41, 1001. https://doi.org/10.1029/2001RG000107.

Ekström, G., 1994. Anomalous earthquakes on volcano ring-fault structures. Earth Planet. Sci. Lett. 128, 707–712. https://doi.org/10.1016/0012-821X(94)90184-8.

Fialko, Y., Khazan, Y., Simons, M., 2001a. Deformation due to a pressurized horizontal circular crack in an elastic half-space, with applications to volcano geodesy. Geophys. J. Int. 146, 181–190. https://doi.org/10.1046/j.1365-246X.2001.00452.x.

Fialko, Y., Simons, M., Khazan, Y., 2001b. Finite source modelling of magmatic unrest in Socorro, New Mexico, and Long Valley, California. Geophys. J. Int. 146, 191–200. https://doi.org/10.1046/j.1365-246X.2001.00453.x.

Galland, O., Bertelsen, H.S., Guldstrand, F., Girod, L., Johannessen, R.F., Bjugger, F., Burchardt, S., Mair, K., 2016. Application of open-source photogrammetric software MicMac for monitoring surface deformation in laboratory models. J. Geophys. Res., Solid Earth 121, 2852–2872. https://doi.org/10.1002/2015JB012564.

Galland, O., Holohan, E., van Wyk de Vries, B., Burchardt, S., 2018. Laboratory Modelling of Volcano Plumbing Systems: A Review. Advances in Volcanology. Springer, Cham, pp. 147–214.

Geshi, N., Shimano, T., Chiba, T., Nakada, S., 2002. Caldera collapse during the 2000 eruption of Miyakejima Volcano, Japan. Bull. Volcanol. 64, 55–68. https://doi.org/10.1007/s00445-001-0184-z.

Geyer, A., Folch, A., Martí, J., 2006. Relationship between caldera collapse and magma chamber withdrawal: an experimental approach. J. Volcanol. Geotherm. Res. 157, 375–386. https://doi.org/10.1016/J.JVOLGEORES.2006.05.001.

Gudmundsson, M.T., Jónsdóttir, K., Hooper, A., Holohan, E.P., Halldórsson, S.A., Ófeigsson, B.G., Cesca, S., Vogfjörd, K.S., Sigmundsson, F., Högnadóttir, T., Einarsson, P., Sigmarsson, O., Jarosch, A.H., Jónasson, K., Magnússon, E., Hreinsdóttir, S., Bagnardi, M., Parks, M.M., Hjörleifsdóttir, V., Pálsson, F., Walter, T.R., Schöpfer, M.P.J., Heimann, S., Reynolds, H.I., Dumont, S., Bali, E., Gudfinnsson, G.H., Dahm, T., Roberts, M.J., Hensch, M., Belart, J.M.C., Spaans, K., Jakobsson, S., Gudmundsson, G.B., Fridriksdóttir, H.M., Drouin, V., Dürig, T., Adalgeirsdóttir, G., Riishuus, M.S., Pedersen, G.B.M., Van Boeckel, T., Oddsson, B., Pfeffer, M.A., Barsotti, S., Bergsson, B., Donovan, A., Burton, M.R., Aiuppa, A., 2016. Gradual caldera collapse at Bárdarbunga volcano, Iceland, regulated by lateral magma outflow. Science 353 (6296), aaf8988. https://doi.org/10.1126/science.aaf8988.

Holohan, E.P., Van Wyk de Vries, B., Troll, V.R., 2008. Analogue models of caldera collapse in strike-slip tectonic regimes. Bull. Volcanol. 70, 773–796. https://doi.org/10.1007/s00445-007-0166-x.

Holohan, E.P., Schöpfer, M.P.J., Walsh, J.J., 2011. Mechanical and geometric controls on the structural evolution of pit crater and caldera subsidence. J. Geophys. Res., Solid Earth 116, B07202. https://doi.org/10.1029/2010JB008032.

Holohan, E.P., Sudhaus, H., Walter, T.R., Schöpfer, M.P.J., Walsh, J.J., 2017. Effects of host-rock fracturing on elastic-deformation source models of volcano deflation. Sci. Rep. 7, 10970. https://doi.org/10.1038/s41598-017-10009-6.

Howard, K.A., 2010. Caldera collapse: perspectives from comparing Galápagos volcanoes, nuclear-test sinks, sandbox models, and volcanoes on Mars. GSA Today 20, 4–10. https://doi.org/10.1130/GSATG82A.1.

Jónsson, S., Zebker, H., Amelung, F., 2005. On trapdoor faulting at Sierra Negra volcano, Galápagos. J. Volcanol. Geotherm. Res. 144, 59–71. https://doi.org/10.1016/j.jvolgeores.2004.11.029.

Maerten, F., Maerten, L., Cooke, M., 2010. Solving 3D boundary element problems using constrained iterative approach. Comput. Geosci. 14, 551–564. https://doi.org/10.1007/s10596-009-9170-x.

Manconi, A., Walter, T.R., Amelung, F., 2007. Effects of mechanical layering on volcano deformation. Geophys. J. Int. 170, 952–958. https://doi.org/10.1111/j.1365-246X.2007.03449.x.

Michon, L., Staudacher, T., Ferrazzini, V., Bachèlery, P., Marti, J., 2007. April 2007 collapse of Piton de la Fournaise: a new example of caldera formation. Geophys. Res. Lett. 34, L21301. https://doi.org/10.1029/2007GL031248.

Mori, J., McKee, C., 1987. Outward-dipping ring-fault structure at Rabaul Caldera as shown by earthquake locations (Papua New Guinea). Science 235 (4785), 193–195. https://doi.org/10.1126/science.235.4785.193.

Mori, J., White, R.A., Harlow, D.H., Okubo, P., Power, J.A., Hoblitt, R.P., Laguerta, E.P., Lanuza, A., Bautista, B.C., 1996. Volcanic earthquakes following the 1991 climactic eruption of Mount Pinatubo: strong seismicity during a waning eruption. In: Fire and Mud: Eruptions and Lahars of Mt. Pinatubo, Philippines, pp. 339–350.

Neal, C.A., Tollett, W., Nadeau, P.A., Zoeller, M.H., Swanson, D.A., Cappos, M., Elias, T., Werner, C., Hazlett, R., Okubo, P., Coombs, M., Lerner, A.H., Dietterich, H.R., Ball, J.L., Clor, L., Lundgren, P., Desmither, L., Bard, J., Moniz, C.J., Montgomery-Brown, E.K., Fuke, S., Anderson, K.R., Trusdell, F., Conway, S., Kauahikaua, J., Houghton, B.F., Kamibayashi, K., Pekalib, S., Neal, C.A., Gansecki, C., Younger, E.F., Chang, J.C., Orr, T., Miklius, A., Million, W., Waite, G., Fukunaga, P., Fisher, G., Antolik, L., Babb, J.L., Calles, K., Dotray, P., Damby, D., Cervelli, P.F., Brantley, S.R., Thelen, W.A., Burgess, M., Poland, M.P., Diefenbach, A.K., Shiro, B., Mulliken, K., Kelly, P., Kern, C., Parcheta, C., Patrick, M.R., Johanson, I.A., 2018. The 2018 rift eruption and summit collapse of Kīlauea Volcano. Science eaav7046, 1–14. https://doi.org/10.1126/science.aav7046.

Nettles, M., Ekström, G., 1998. Faulting mechanism of anomalous earthquakes near Bárdarbunga Volcano, Iceland. J. Geophys. Res. 103, 17973. https://doi.org/10.1029/98JB01392.

Nikkhoo, M., Walter, T.R., 2015. Triangular dislocation: an analytical, artefact-free solution. Geophys. J. Int. 201, 1119–1141. https://doi.org/10.1093/gji/ggv035.
Norini, G., Acocella, V., 2011. Analogue modeling of flank instability at Mount Etna: understanding the driving factors. J. Geophys. Res., Solid Earth 116, B07206. https://doi.org/10.1029/2011JB008216.
Peltier, A., Staudacher, T., Bachèlery, P., Cayol, V., 2009. Formation of the April 2007 caldera collapse at Piton de La Fournaise volcano: insights from GPS data. J. Volcanol. Geotherm. Res. 184, 152–163. https://doi.org/10.1016/j.jvolgeores.2008.09.009.
Poland, M., Hamburger, M., Newman, A., 2006. The changing shapes of active volcanoes: history, evolution, and future challenges for volcano geodesy. J. Volcanol. Geotherm. Res. https://doi.org/10.1016/j.jvolgeores.2005.11.005.
Pyle, D.M., Mather, T.A., Biggs, J., 2013. Remote sensing of volcanoes and volcanic processes: integrating observation and modelling – introduction. Geol. Soc. (Lond.) Spec. Publ. 380, 1–13. https://doi.org/10.1144/SP380.14.
Riel, B., Milillo, P., Simons, M., Lundgren, P., Kanamori, H., Samsonov, S., 2015. The collapse of Bárðarbunga caldera, Iceland. Geophys. J. Int. 202, 446–453. https://doi.org/10.1093/gji/ggv157.
Roche, O., Druitt, T.H., Merle, O., 2000. Experimental study of caldera formation. J. Geophys. Res. 105, 395–416. https://doi.org/10.1029/1999JB900298.
Roche, O., Van Wyk De Vries, B., Druitt, T.H., 2001. Sub-surface structures and collapse mechanisms of summit pit craters. J. Volcanol. Geotherm. Res. 105, 1–18. https://doi.org/10.1016/S0377-0273(00)00248-1.
Ruch, J., Acocella, V., Geshi, N., Nobile, A., Corbi, F., 2012. Kinematic analysis of vertical collapse on volcanoes using experimental models time series. J. Geophys. Res., Solid Earth 117 (B7). https://doi.org/10.1029/2012JB009229.
Saunders, S.J., 2001. The shallow plumbing system of Rabaul caldera: a partially intruded ring fault? Bull. Volcanol. 63, 406–420. https://doi.org/10.1007/s004450100159.
Segall, P., 2010. Earthquake and Volcano Deformation. Princeton University Press.
Thielicke, W., Stamhuis, E.J., 2014. PIVlab – towards user-friendly, affordable and accurate digital particle image velocimetry in MATLAB. J. Open Res. Softw. 2. https://doi.org/10.5334/jors.bl.
Trasatti, E., Giunchi, C., Bonafede, M., 2005. Structural and rheological constraints on source depth and overpressure estimates at the Campi Flegrei caldera, Italy. J. Volcanol. Geotherm. Res. 144, 105–118. https://doi.org/10.1016/j.jvolgeores.2004.11.019.
Trasatti, E., Giunchi, C., Bonafede, M., 2003. Effects of topography and rheological layering on ground deformation in volcanic regions. J. Volcanol. Geotherm. Res. 122, 89–110. https://doi.org/10.1016/S0377-0273(02)00473-0.
Xu, W., Jónsson, S., Ruch, J., Aoki, Y., 2016. The 2015 Wolf volcano (Galápagos) eruption studied using Sentinel-1 and ALOS-2 data: the 2015 Wolf eruption in the Galápagos. Geophys. Res. Lett. 43, 9573–9580. https://doi.org/10.1002/2016GL069820.
Yun, S., Segall, P., Zebker, H., 2006. Constraints on magma chamber geometry at Sierra Negra Volcano, Galápagos Islands, based on InSAR observations. J. Volcanol. Geotherm. Res. 150, 232–243. https://doi.org/10.1016/j.jvolgeores.2005.07.009.